frontiers | Frontiers in Soft Matter

TYPE Original Research
PUBLISHED 19 January 2024
DOI 10.3389/frsfm.2023.1339496

OPEN ACCESS

EDITED BY
Jay X. Tang,
Brown University, United States

REVIEWED BY
Anne-Laure Fameau,
Institut National de Recherche pour l'Agriculture, l'Alimentation et l'Environnement (INRAE), France
Oscar Domenech,
University of Barcelona, Spain

*CORRESPONDENCE
Marité Cárdenas,
marite.cardenas@mau.se,
marite.cardenas@ehu.eus
Ali Miserez,
ali.miserez@ntu.edu.sg

RECEIVED 16 November 2023
ACCEPTED 31 December 2023
PUBLISHED 19 January 2024

CITATION
Gudlur S, Ferreira FV, Ting JSM, Domene C, Maricar S, Le Brun AP, Yepuri N, Moir M, Russell R, Darwish T, Miserez A and Cárdenas M (2024), pH-dependent interactions of coacervate-forming histidine-rich peptide with model lipid membranes.
Front. Soft Matter 3:1339496.
doi: 10.3389/frsfm.2023.1339496

pH-dependent interactions of coacervate-forming histidine-rich peptide with model lipid membranes

Sushanth Gudlur[1], Filipe Viana Ferreira[1], Javier Shu Ming Ting[2], Carmen Domene[3], Syed Maricar[1], Anton P. Le Brun[4], Nageshwar Yepuri[5], Michael Moir[5], Robert Russell[5], Tamim Darwish[5], Ali Miserez[1,2]* and Marité Cárdenas[2,6,7,8]*

[1]Biological and Biomimetic Materials Laboratory (BBML), Center for Sustainable Materials (SusMat), School of Materials Science and Engineering, Nanyang Technological University (NTU), Singapore, Singapore, [2]School of Biological Sciences, Nanyang Technological University (NTU), Singapore, Singapore, [3]Department of Chemistry, University of Bath, Claverton Down, Bath, United Kingdom, [4]Australian Centre for Neutron Scattering, Australian Nuclear Science and Technology Organisation (ANSTO), Lucas Heights, NSW, Australia, [5]National Deuteration Facility (NDF), Australian Nuclear Science and Technology Organisation (ANSTO), Lucas Heights, NSW, Australia, [6]Department of Biomedical Sciences, Biofilm Research Center for Biointerfaces, Malmö University, Malmö, Sweden, [7]Instituto Biofisika (CSIC, UPV/EHU), Fundación Biofísica Bizkaia/Biofisika Bizkaia Fundazioa (FBB), Leioa, Spain, [8]Ikerbasque, Basque Foundation for Science, Bilbao, Spain

Peptide-based liquid droplets (coacervates) produced by spontaneous liquid-liquid phase separation (LLPS), have emerged as a promising class of drug delivery systems due to their high entrapping efficiency and the simplicity of their formulation. However, the detailed mechanisms governing their interaction with cell membranes and cellular uptake remain poorly understood. In this study, we investigated the interactions of peptide coacervates composed of HB*pep*—peptide derived from the histidine-rich beak proteins (HBPs) of the Humboldt squid—with model cellular membranes in the form of supported lipid bilayers (SLBs). We employed quartz crystal microbalance with dissipation monitoring (QCM-D), neutron reflectometry (NR) and atomistic molecular dynamics (MD) simulations to reveal the nature of these interactions in the absence of fluorescent labels or tags. HB*pep* forms small oligomers at pH 6 whereas it forms μm-sized coacervates at physiological pH. Our findings reveal that both HB*pep* oligomers and HB*pep*-coacervates adsorb onto SLBs at pH 6 and 7.4, respectively. At pH 6, when the peptide carries a net positive charge, HB*pep* oligomers insert into the SLB, facilitated by the peptide's interactions with the charged lipids and cholesterol. Importantly, however, HB*pep* coacervate adsorption at physiological pH, when it is largely uncharged, is fully reversible, suggesting no significant lipid bilayer rearrangement. HB*pep* coacervates, previously identified as efficient drug delivery vehicles, do not interact with the lipid membrane in the same manner as traditional cationic drug delivery systems or cell-penetrating peptides. Based on our findings, HB*pep* coacervates at physiological pH cannot cross the cell membrane by a simple passive mechanism and are thus likely to adopt a non-canonical cell entry pathway.

KEYWORDS

LLPS, peptide coacervates, neutron reflectivity, membrane interaction, model membrane, molecular dynamic simulations, supported lipid bilayers

1 Introduction

Peptide-based liquid droplets, also known as coacervates, assembled by liquid-liquid phase separation (LLPS) have emerged as a new class of therapeutic delivery vehicles (Liu et al., 2023). Their attractiveness stems from their exceptionally high entrapping efficiency (Lim et al., 2018; Lim et al., 2020), their versatility in entrapping a broad variety of large macromolecular therapeutics (Sun et al., 2022), and their simple formulation methodology that avoids the use of organic solvents. Depending on the peptide design, the formation and disassembly of these liquid droplets can be controlled via various external triggers such as pH, temperature, ionic strength, etc. This versatility has led to the development of stimuli-responsive peptide coacervates whose delivery into various cell types *in vitro* have resulted in comparable or superior outcomes to those achieved with lipid- and polymer-based nanoparticles (Sun et al., 2022; Sun et al., 2023).

In contrast to well-studied drug delivery platforms, such as lipid- (e.g., liposomes, lipid nanoparticles, nanostructured lipid carriers, etc.) and nanoparticle-based vehicles (e.g., polymeric, cationic, metallic and carbon-based, etc.), mechanistic understanding related to coacervate/cell membrane interactions and their subsequent cellular uptake remains largely incomplete. Current understanding indicates that coacervates, characterized as dense, viscoelastic, μm-sized liquid droplets, exert sufficient compressive stresses to bend the plasma membrane inward (Yuan et al., 2021). Additional factors reported to be involved in coacervate interactions with the membrane surface, and possibly contributing to their cellular uptake, include membrane wetting (partial or complete) (Lu et al., 2022), capillary force generation (Gouveia et al., 2022) and free energy release through adhesion between viscoelastic media (Bergeron-Sandoval et al., 2021).

The specific route of cellular uptake of drug delivery vehicles depends on several factors, including its size, shape, composition, surface charge, hydrophobicity or hydrophilicity, and the specific cell type into which they are delivered (Behzadi et al. 2017). Endocytosis, an umbrella term covering multiple different pathways and mechanisms for cellular entry, is the principal route of entry for most delivery systems into cells (Jones et al., 2003; Kazmierczak et al., 2020). In this regard, charge-based interactions at the plasma membrane, while not the exclusive mode of interaction, often play a significant role in the initial stages of endocytosis, with either beneficial or detrimental implications for the cellular uptake of the delivery vehicle (Harush-Frenkel et al., 2008; Vedadghavami et al., 2020; Gyanani and Goswami, 2023; Spleis et al., 2023).

On one hand, the surface charge on the delivery vehicle can facilitate endocytosis by inducing local deformations in the membrane, causing the membrane to bend or wrap around it (Harush-Frenkel et al., 2008). Such deformations can promote the formation of membrane invaginations that are characteristic of endocytosis. In addition, these interactions could promote other types of chemical interactions, or assist in binding to specific receptors on the cell membrane. On the other hand, surface charge-bearing delivery vehicles and cell-penetrating peptides have the ability to destabilize cell membranes through electrostatic interactions (Thoren et al., 2005; Herce and Garcia, 2007; Rehman et al., 2013). Such interactions can induce changes in lipid organization and fluidity, as well as the formation of transient nanoparticle-induced pores (Karal et al., 2015). Moreover, the disruptive effects of cationic nanoparticles on the cell membrane can trigger cellular responses, such as membrane repair mechanisms and changes in membrane protein activity (Stewart et al., 2018). These cellular responses could, in turn, impact cellular uptake processes and intracellular signaling pathways. Gaining insights into these interactions can guide the design and optimization of delivery systems for enhanced therapeutic efficacy.

In our most recent work, we discovered that HeLa and HepG2 cells internalized simple coacervates–comprised of a single peptide type–mainly through a cholesterol-dependent, non-canonical cell entry pathway involving cytoskeleton rearrangement and filipodia-like protrusions that capture the coacervates (Shebanova et al., 2022). However, to enable live cell imaging, the study employed enhanced green fluorescent protein (EGFP) as a client molecule, which is spatially distributed both in the interior and at the corona of peptide coacervates. In general, client molecules located near the outside surface of coacervates could potentially alter the overall surface charge (Welsh et al., 2022), form layered droplets (Boeynaems et al., 2019; Latham and Zhang, 2022) and affect interfacial tension (Wang et al., 2023) thereby influencing coacervate interaction with lipid membranes and cellular uptake in ways that we still do not understand. Whether these interfacial interactions mediated by client molecules significantly influence cellular uptake remained unexplored in our previous work.

In this study, we employ quartz crystal microbalance with dissipation monitoring (QCM-D), neutron reflectometry (NR) and atomistic molecular dynamic (MD) simulations to investigate peptide coacervate interactions with model membranes, in the absence of client molecules. The aforementioned techniques enable direct monitoring of coacervate-membrane interactions without the potential influence of fluorescently-labelled cargos or other types of client molecules. QCM-D and NR are complementary surface sensitive techniques, offering insights into both the overall adsorption processes occurring at the model membrane surface and detailed structural information about the membrane, including changes in composition of the lipid bilayer tail region, due to peptide incorporation or solvent penetration (Clifton et al., 2020). The nature of the interaction is verified by MD simulations, which provide a complementary picture to NR measurements.

2 Materials and methods

2.1 Materials

All peptides were purchased as lyophilized powder and certified >95% purity from GL Biochem (Shanghai) Ltd., China. Monobasic sodium phosphate (NaH_2PO_4), dibasic sodium phosphate (Na_2HPO_4), tribasic sodium phosphate (Na_3PO_4), sodium chloride (NaCl), Corning® black 384 transparent-bottom plates were purchased from Sigma-Aldrich (Singapore). Deuterated phospholipids and deuterated cholesterol were synthetized by ANSTO's National Deuteration Facility. Isopropyl alcohol, cholesterol and non-deuterated phospholipids used in QCM-D and SLB experiments were purchased from Sigma Aldrich (Singapore), QCM-D sensors were acquired from Biolin Scientific

AB (Gothenburg, Sweden). Silicon wafers for NR were purchased from El-Cat Inc. (NJ, United States).

2.2 Turbidity measurements for peptide concentration and pH profile

Stock solutions of HB*pep* peptide were prepared by solubilizing the lyophilized peptide directly in 10 mM acetic acid to achieve a final peptide concentration of 10 mg/mL. At this low pH (~3), the peptides remain largely monomeric and do not coacervate. Sodium phosphate buffer solutions (10 mM, 154 mM NaCl final concentration) with pH ranging between 2-11 were prepared by mixing appropriate volumes of NaH_2PO_4, Na_2HPO_4, and Na_3PO_4 stock solutions to achieve the desired pH, which were later confirmed using a pH meter (Mettler Toledo, Singapore) before and after the addition of peptide stock solutions. For determining the concentration range within which HB*pep* coacervate, 11 different samples were prepared in a 38-well transparent-bottom microtiter plate by diluting the peptide stock solution into sodium phosphate buffer (pH 7.4) such that the final peptide concentration varied between 0 and 1 mg/mL in 0.1 mg/mL increments and a final volume of 100 µL. The volume of 10 mM acetic acid was kept constant in all the above samples. Immediately after the addition of the peptide, the absorbance of the samples were collected between 400 and 800 nm using a Tecan Spark (Männedorf, Switzerland) multimode plate reader. The mean of the absorbance values at 600 nm (A_{600}) for each sample, collected from three separate experiments, was plotted against the corresponding peptide concentration and fitted to a dose response curve using OriginPro 2021. Error bars indicate standard error of the mean. For characterizing the pH range within which HB*pep* coacervate, samples were prepared in a 38-well transparent-bottom microtiter plates by diluting the peptide stock solution into sodium phosphate buffer (10 mM, 154 mM NaCl) of varying pH such that the final pH of the sample varied between 2-11 in small increments and a final volume of 100 µL. Absorbance of the samples was collected and the data plotted as described above.

2.3 Dynamic light scattering (DLS) measurements

All DLS measurements were carried out in a Malvern Zetasizer Nano ZS (Malvern Panalytical Ltd., Singapore). HB*pep* coacervates were prepared in a quartz cuvette (10 mm pathlength) by diluting the peptide stock solution that was previously dissolved in 10 mM acetic acid, into sodium phosphate buffer (pH 6, 7.4 or 8) such that the final peptide concentration was 0.1, 0.25, 0.5 or 1 mg/mL. DLS measurements were conducted at a 173° detection angle for 60 min at a fixed temperature of 25°C. Data was plotted using OriginPro 2021. Experiments were done in duplicates.

2.4 Differential interference contrast (DIC) microscopy

About 20 µL of the peptide solution of various (0.1–1 mg/mL) concentrations prepared in sodium phosphate buffer (10 mM, 154 mM NaCl, pH 7.4) was pipetted on to the cover glass of a MatTek dish (cover glass No. 1.5) and the sample imaged using a Carl Zeiss Axio Observer Z1–Inverted Microscope fitted with a motorized stage and an EC Plan-Neofluar 63x/1.25 oil, FWD 0.1 mm, CG 0.17 mm (DIC) objective. All images were collected using an AxioCam MRm CCD camera, 1,388 × 1,040 pixels, 6.45 µm/pixel. All images were acquired using Zen 2 (blue) software and processed using ImageJ2 (version 2.3.0/1.53f). Experiments were done in duplicates.

2.5 Deuterated lipids

2.5.1 DOPG-d_{66} (94 ± 2% D)

We report here the production of sub-gram quantities of tail deuterated 1,2-dioleoyl-d_{66}-*sn*-glycero-3-phospho-(1′-*sn*-glycerol) (DOPG-d_{66}) and its structural characterization. Oleic acid-d_{33}, a precursor for the synthesis, was produced using our previously reported methods (Darwish et al., 2013). The primary and secondary hydroxyl groups of 3-benzyloxy-*sn*-glycerol (at sn-1 and sn-2) were esterified using deuterated oleic acid-d_{33} in the presence of dicyclohexylcarbodiimide (DCC) and a catalytic amount of 4-dimethylaminopyridine (DMAP). The benzyl group was removed using boron trichloride to afford 1,2-dioleoyl-d_{66}-*sn*-glycerol. The free alcohol was phosphorylated with phosphorus oxychloride, to give the corresponding 1,2-diacyl phosphatidic dichloride, which was used in the next step without further purification. Coupling of the phosphatidic dichloride with 1,2-isopropylidene-*sn*-glycerol in the presence of the anhydrous pyridine afforded acetonide protected DOPG-d_{66}. The protecting group was cleaved under mild acidic conditions to give DOPG-d_{66} as colourless waxy solid.

2.5.2 POPC-d_{64} (94 ± 2% D)

1-Palmitoyl-d_{31}-2-oleoyl-d_{33}-glycero-3-phosphocholine (POPC-d_{64}) was produced using previously reported methods for the synthesis of mixed acyl glycerophospholipids (Moir et al., 2022) from palmitic acid-d_{31} and oleic acid-d_{33} (Darwish et al., 2013).

2.5.3 Cholesterol-d_{45} (80 ± 2% D)

Deuterated cholesterol (average 80% D as determined by mass spectrometry) was produced using previously reported methods (Sebastiani et al., 2021; Recsei et al., 2023) (ca. 90% D_2O in the growth medium).

2.6 Quartz crystal microbalance with dissipation monitoring (QCM-D)

Measurements were performed using a Q-SENSE E4 system (Q-Sense, Sweden) connected to an Ismatec peristaltic pump model ISM596D. The 50 nm SiO_2 coated Au sensors were cleaned in 2 v/v % Hellmanex under bath sonication for 10 min, followed by extensive rinsing with MilliQ water and ethanol. The sensors were dried under N_2 flow and subjected to oxygen plasma cleaning for 2 min in a Harrick plasma cleaner (Model No. PDC-002, Harrick Plasma Inc. United States) fitted with a gas flow mixer (PLASMAFLO PDC-FMG, Harrick Plasma Inc. United States) for

controlling oxygen flow rate. A lipid vesicle suspension was prepared at 0.2 mg/mL in MilliQ water (hydrodynamic diameter smaller than 50 nm as confirmed by DLS, prepared by tip sonication in H_2O). The composition of the lipid vesicles was 1-palmitoyl-2-oleoyl-sn-glycero-3-phosphocholine (POPC), 1-palmitoyl-2-oleoyl-sn-glycero-3-[phospho-rac-(1-glycerol)] (POPG) and cholesterol (POPC:POPG:Cholesterol) at a 7:1:2 molar ratio. This composition was chosen to represent the overall charge of mammalian cells (Virtanen et al., 1998). The lipid films were prepared by mixing appropriate amounts of lipids from chloroform stocks and gently evaporating the solvent under N_2 flow and rotation, and finally subjecting to vacuum for at least 1 h.

Prior to experiments, the fundamental frequency (5 MHz) and five overtones (3rd, 5th, 7th, 9th, and 11th) were found and recorded in MilliQ water. The flow rate was set to 0.1 mL/min, and the temperature was controlled as specified. A baseline was obtained in MilliQ water prior to injection of the vesicle solution (the lipid vesicle suspension was mixed in a 1:1 volume ratio with 4 mM $CaCl_2$ just prior injection into the solid-liquid cells). A constant flow of vesicles was maintained until stable signals were obtained before rinsing with excess MilliQ water. The supported lipid bilayers (SLBs) gave signals of typically -24-25 Hz and 0.2–0.4 ppm in dissipation, in line with previous results (Clifton et al., 2020). Rinsing with 10 mM phosphate buffer enriched with 154 mM NaCl at pH 7.4 or pH 6 was performed. HB*pep* coacervates (0.25 mg/mL) were formed and incubated for 5 min prior to addition to the SLBs. QCM-D measurements were performed in duplicates. For measurements in which coacervate sedimentation was avoided, the instrument was set upside down as previously done for other systems (Lind et al., 2019).

2.7 Supported lipid bilayers on glass

The supported lipid bilayers (SLBs) were prepared on a glass coverslip in a microfluidic chip by the solvent-assisted method reported by Ferhan et al. (2019) with slight modifications. To clean and hydrophilize the glass surface, the coverslip was soaked overnight in a 1 v/v% solution of Hellmanex, washed with MilliQ water and ethanol, dried in an oven then subjected to oxygen plasma cleaning for 2 min in a Harrick plasma cleaner (Model No. PDC-002, Harrick Plasma Inc. United States) fitted with a gas flow mixer (PLASMAFLO PDC-FMG, Harrick Plasma Inc. United States) for controlling oxygen flow rate. Immediately after this, the coverslip was attached to a multichannel microfluidic chip (Ibidi sticky-Slide VI0.4), and all microfluidic channels were filled with MilliQ water. The chip has six microfluidic channels, each with a length of 17 mm, a width of 3.8 mm and a height of 400 µm.

To prepare the lipid solution, POPC, cholesterol and two fluorescent markers, namely, 18:1 Liss Rhod PE and 25-NBD cholesterol (that selectively mix with POPC and cholesterol, respectively), were solubilized in isopropanol, while POPG was solubilized in ethanol. Appropriate amounts of each of those five components were mixed and diluted in water:isopropanol with 1:1 volume ratio to create a 0.4 mg/mL POPC:POPG:Cholesterol solution with a 7:1:2 molar fraction. Liss Rhod PE and NBD cholesterol were used at a concentration of 3.4 µg/mL and 1.8 µg/mL, respectively.

To create a SLB, an Ismatec peristaltic pump model ISM596D was used. First, water:isopropanol with a 1:1 volume ratio was pumped for several minutes to ensure complete exchange of the MilliQ water that previously filled the channel. Then, the lipid solution was pumped for 10 min at 50 µL/min, the flow was stopped for 5 min, and MilliQ water was pumped, also for 10 min at 50 µL/min. The resulting SLB homogeneously and completely covered the glass substrate in the microfluidic channel.

The coacervate experiment was then carried out just as in the QCM-D, the only difference being the reduced flow rate of 50 µL/min. Images were collected as the experiment was ongoing in a Carl Zeiss Axio Observer Z1 inverted fluorescence microscope fitted with a motorized stage and a Plan-Apochromat 63x/1.40 oil DIC, FWD 0.19 mm, CG 0.17 objective. All images were acquired using a Carl Zeiss AxioCam 503 Mono camera, 1,936 × 1,460 pixels, 72 nm/pixel using Zen 2 (blue) software and processed using ImageJ2 (version 2.9.0/1.54f).

2.8 Neutron reflection (NR)

Experiments were performed on the reflectometer SPATZ at the Australian Nuclear Science and Technology Organisation (ANSTO) using a setup for solid/liquid interfaces (Le Brun et al., 2023). The momentum transfer range and momentum transfer (Q) resolution used was 0.011 $Å^{-1}$ < Q < 0.273 $Å^{-1}$ and $\Delta Q/Q$ = 5.8%, respectively. The instrument uses the time-of-flight principle and a disc chopper pairing of discs 1 and 2 set 480 mm apart running at 25 Hz was used (2.5 Å < λ < 20 Å). Collimation slits used were set to 2.66 mm and 0.75 mm for an angle of incidence of 0.85° and 10.94 mm and 3.09 mm for 3.5°, providing an illuminated footprint of 55 mm along the beam. Data was reduced with the *refnx* software package (Nelson and Prescott, 2019) where the time-of-flight is converted to wavelength which is used to calculate Q, accounts for detector efficiency, re-bins the data to instrument resolution, subtracts the background, stiches the data from the two angles of incidence together at the appropriate overlap region, and scales the data so that the reflectivity at the critical edge is equal to 1.

The silicon blocks (100) of 100 mm diameter and 10 mm thickness and O-rings (TEFLON of 100 µm thickness) were cleaned in the following series of solvents: 2% Hellmanex for at least 1 h followed by extensive rinsing with MilliQ water. Before assembling the cells, the blocks were dried with a flow of nitrogen gas and exposed for 30 min to ozone to finally be assembled in dry conditions. During the assembling, the substrate was sealed with the polished surface in contact with the liquid using a thin Teflon O-ring, and the cells were connected to an HPLC pump to allow the exchange of solvent with D_2O, H_2O, and CMSi (38:62 v/v D_2O: H_2O).

The solid/liquid cells were pre-equilibrated to 25°C using a circulating water bath and the surfaces were characterized in H_2O and D_2O to determine the roughness and the thickness of the silicon oxide layer. Then, the SLBs were formed using vesicle fusion as described in Section 2.6, and characterized in three isotropic contrasts composed of H_2O based-, D_2O based, and CMSi-based (38:62 D_2O: H_2O (v/v)) buffer. The composition of the lipid vesicles was POPC-d_{64}:DOPG-d_{66}:Cholesterol-d_{45} at a 7:1:2 molar ratio. Here, d_{64}:DOPG was used since synthesis of tail

deuterated POPG has not been reported or performed to the date of publication. The lipid films were prepared by mixing appropriate amounts of lipids from chloroform stocks and gently evaporating the solvent under N_2 flow and rotation, and finally subjecting to vacuum for at least 1 h.

The SLBs were fitted using a 4-layer model constituted by the oxide layer and three layers that correspond to the heads-tails-heads of the lipid membrane. During the data fitting, the lipid bilayer was constrained to be symmetric, that is, the coverage, the thickness, and the scattering length density (SLD) of the heads were the same for both leaflets. Additionally, the roughness was constrained to be the same across the whole bilayer. The HB*pep* peptide was slowly introduced via a syringe at concentrations of 0.25 mg/mL in the corresponding buffer, upon re-equilibration of ~5 min. After roughly 1 h 20 min of incubation, the samples were rinsed with H_2O based buffer and re-characterized in all three contrasts by using 1/10 of the final peptide concentration. Data was collected prior and after buffer exchange in H_2O based buffer and no changes in reflectivity were observed.

To fit the data in the three isotropic contrasts after protein incubation and rinsing, the head-group thickness and coverage was kept constant but the thickness and SLD of the tails were allowed to vary. A layer of protein was added on top of the SLB. The experiments were performed only once due to the restricted availability of beam time. Data fitting was performed using the MOTOFIT package (Nelson, 2006) and to determine the errors of the fits, a Monte Carlo error analysis was performed using genetic optimization.

2.9 Peptide modeling

The structure of the peptide was built using the PEP-FOLD4 server (Rey et al., 2023; Tufféry and Derreumaux, 2023), which has the advantage over other available servers that it embeds a Debye-Hückel formalism to treat pH conditions and salt concentration variations. Peptide conformations are pH- and salt concentration-dependent, and thus, two systems were considered to mimic neutral and acidic conditions. The main input was the sequence in FASTA format (GHGVY GHGVY GHGPY GHGPY GHGLYW). The forward-backtrack sampling algorithm was selected to sample the structural alphabet profile and the number of models generated was 100. Default parameters related to the Monte Carlo protocol (10,000 steps) and the pseudo-random generator seed were adopted to generate the 3D models. The Debye-Hückel contribution was switched on, and the pH was specified as well as an ionic strength of 154 mM NaCl to match the experimental conditions. The use of the zwitterionic forms of the peptides and the default pKa values of 6 for His residues were used.

2.10 Molecular dynamics simulations

A membrane containing POPC, POPG and cholesterol molecules in a proportion 70:10:20 (POPC:POPG:Cholesterol) was generated using CHARMM-GUI Membrane Builder (Jo et al., 2008; Jo et al., 2009; Wu et al., 2014). The membrane contained 210 POPC molecules, 30 POPG molecules and 60 cholesterol molecules in the mixed bilayer. Subsequently, the multicomponent assembler (Kern et al., 2023) of CHARMM-GUI facilitated to build two all-atom molecular models at neutral or acidic pH, using the first 15 peptides rendered by PEP-FOLD4 (the more favorable energetically), and the previously built complex membrane. The combined system (bilayer and peptides) was then solvated to produce a rectangular box of dimensions (130 × 130 × 100) $Å^3$. Ions were added resulting in a final concentration of 154 mM NaCl (Humphrey et al., 1996). The final system contained over 168,000 atoms. CHARMM22 (Li et al., 2005) parameters (with CMAP correction) were used for the peptides, CHARMM36 for lipids (Klauda et al., 2010), standard parameters for ions (Noskov et al., 2004) and the TIP3P (Jorgensen et al., 1983) model for water. NAMD 3.0alpha GPU (Phillips et al., 2005) and Gromacs 2023 (Berendsen et al., 1995) were employed to calculate the dynamics of the systems throughout (Phillips et al., 2005). Although we started using NAMD, due to performance, we switched to Gromacs. One simulation of the neutral system and one of the charged system were obtained with NAMD, and five replicas per pH were obtained with Gromacs. The total cumulative production time is 12*0.2 μs (2.4 μs).

Initially, 10,000 steps of minimization were performed to remove steric clashes, followed by the progressive removal of constraints at 500 ps intervals to allow for gradual equilibration of the system. Constraints were released in the following order: i) bulk water and lipid tails; ii) lipid head groups; iii) peptide side chains. Unrestrained dynamics was then undertaken in the NPT ensemble. The Particle Mesh Ewald method was used for the treatment of full-system periodic electrostatic interactions; interactions were evaluated every second timestep with a value of 1 Å to determine grid spacing (Darden et al., 1993). Electrostatic and van der Waals forces were calculated every timestep and up to a cutoff distance of 12 Å. A switching distance of 10 Å was chosen to smoothly truncate the non-bonded interactions. Only atoms in a Verlet pair list within a cutoff distance of 13.5 Å were considered, with the list reassigned of reassigned every 20 steps (Verlet, 1967). The SETTLE algorithm was used to constrain all bonds involving hydrogen atoms to allow the use of a 2 fs timestep (Miyamoto and Kollman, 1992). The Nose-Hoover-Langevin piston method was employed to control the pressure with a 200 fs period, 50 fs damping constant and a desired value of 1 atmosphere (Martyna et al., 1994; Feller et al., 1995). The system was coupled to a Nose-Hoover thermostat to sustain a temperature of 298 K throughout.

3 Results and discussion

3.1 Identifying optimal conditions for peptide-coacervate and model cell membrane interactions studies

HB*pep* is a 26-residue peptide inspired by the Histidine-rich beak proteins (HBPs) of the Humboldt squid (Tan et al., 2015). The peptide sequence (GHGVY GHGVY GHGPY GHGPY GHGLY W) consists of five GHGxY repeats, [where x is either valine (V), proline (P) or leucine (L)], and a C-terminal tryptophan residue, both of which are important drivers of phase separation (Figure 1A) (Wang et al., 2018; Gabryelczyk et al., 2019). HB*pep* phase separates under

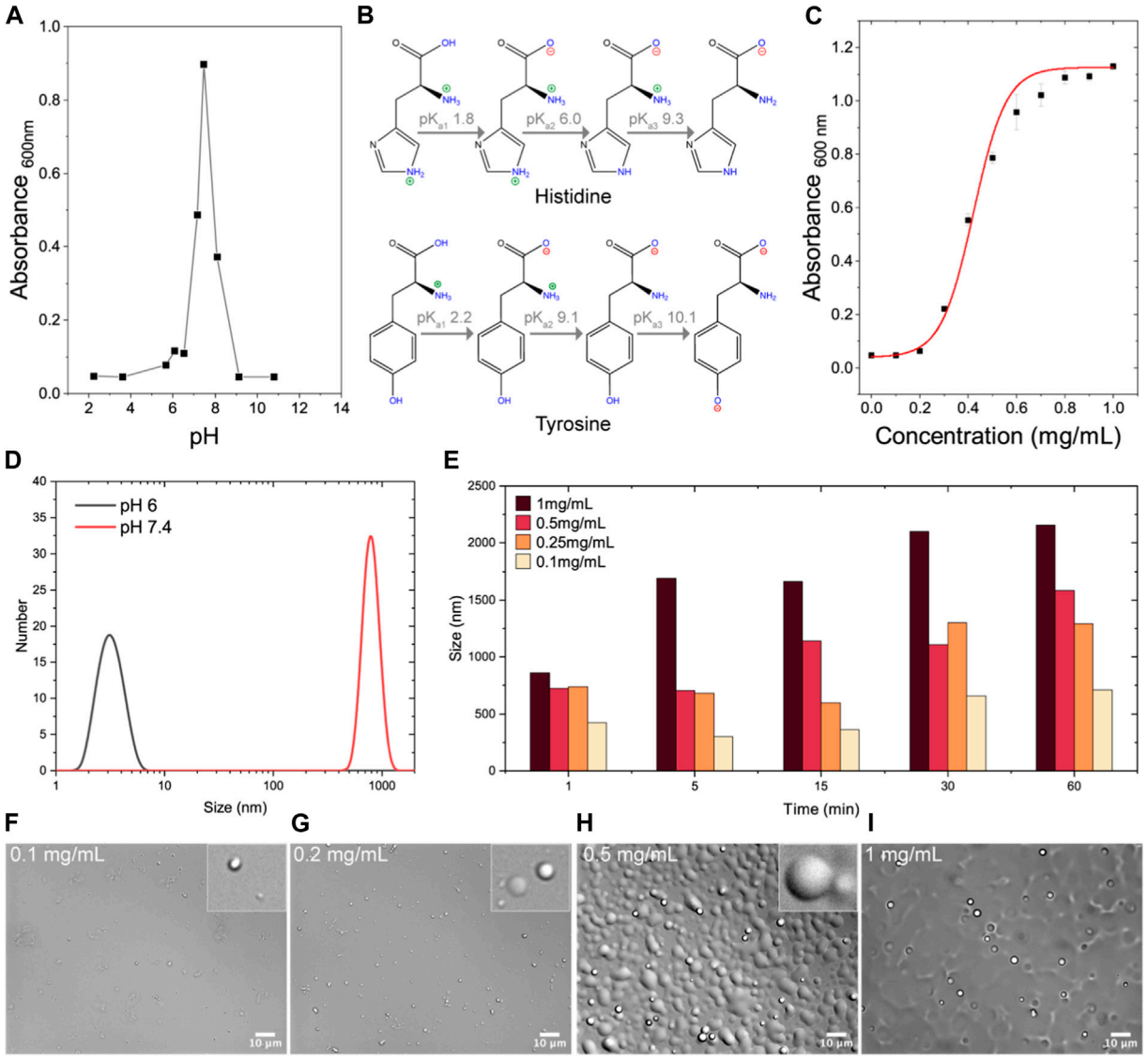

FIGURE 1
Characterization of HB*pep* to determine optimal experimental conditions for HB*pep*-membrane interactions studies. **(A)** Turbidity measurements of HB*pep* (Seq: GHGVY GHGVY GHGPY GHGPY GHGLYW) within a pH range of 2–11 indicate optimal coacervation at physiological pH. **(B)** Different p*K*a values of histidine (top) and tyrosine (bottom) are illustrated to highlight that when the pH is below 6 or above 9, HB*pep* is unable to coacervate due to the positive and negative charge contributions from the histidine and tyrosine side-chains, respectively, resulting in charge-charge repulsion at these pH ranges. **(C)** Turbidity measurements of HB*pep* samples within a concentration range of 0.1–1 mg/mL when prepared at pH 7.4 indicate a concentration-dependent increase in turbidity. **(D)** DLS measurements of HB*pep* samples at pH 6 and 7.4 suggest an oligomeric state at pH 6 and coacervates at pH 7.4. **(E)** DLS measurements of HB*pep* coacervates prepared at pH 7.4 and at four different concentrations when monitored up to 60 min indicate particle size of ~1 µm diameter whose size gradually increased with increasing concentration. **(F–I)** DIC imaging of the HB*pep* samples confirm coacervation and its size-correlation with increasing HB*pep* concentration. The illustration for histidine pKa in C has been recreated with minor modifications from Saurabh et al. (2022), licensed CC-BY-4.0.

physiological conditions into µm-sized coacervate microdroplets that exhibit an extremely high efficiency (>99%) to recruit a wide variety of therapeutics within their dense phase (Lim et al., 2018; Lim et al., 2020). Consequently, HB*pep* and its variant were developed into an intracellular delivery system capable of delivering a wide variety of therapeutics into different cell types *in vitro* with little to no cytotoxicity (Sun et al., 2022).

In order to identify the optimal experimental conditions for investigating HB*pep*-coacervate and model cell membrane interactions, turbidity measurements were carried out with HB*pep* at different conditions of pH and concentrations (Figures 1A, C). In general, coacervation of phase-separating peptides and proteins can occur over a wide pH range and can be monitored by measuring sample turbidity (Supplementary Figure S1), coacervate size (Supplementary Figure S2), or both. However, turbidity measurements—the standard practice in the field—allow for the determination of "phase-separation (a.k.a coacervation) propensity" when the coacervate size remains more or less similar across a pH range. Turbidity measurements of HB*pep* prepared in sodium phosphate buffers spanning a pH range of 2–11, indicated that the

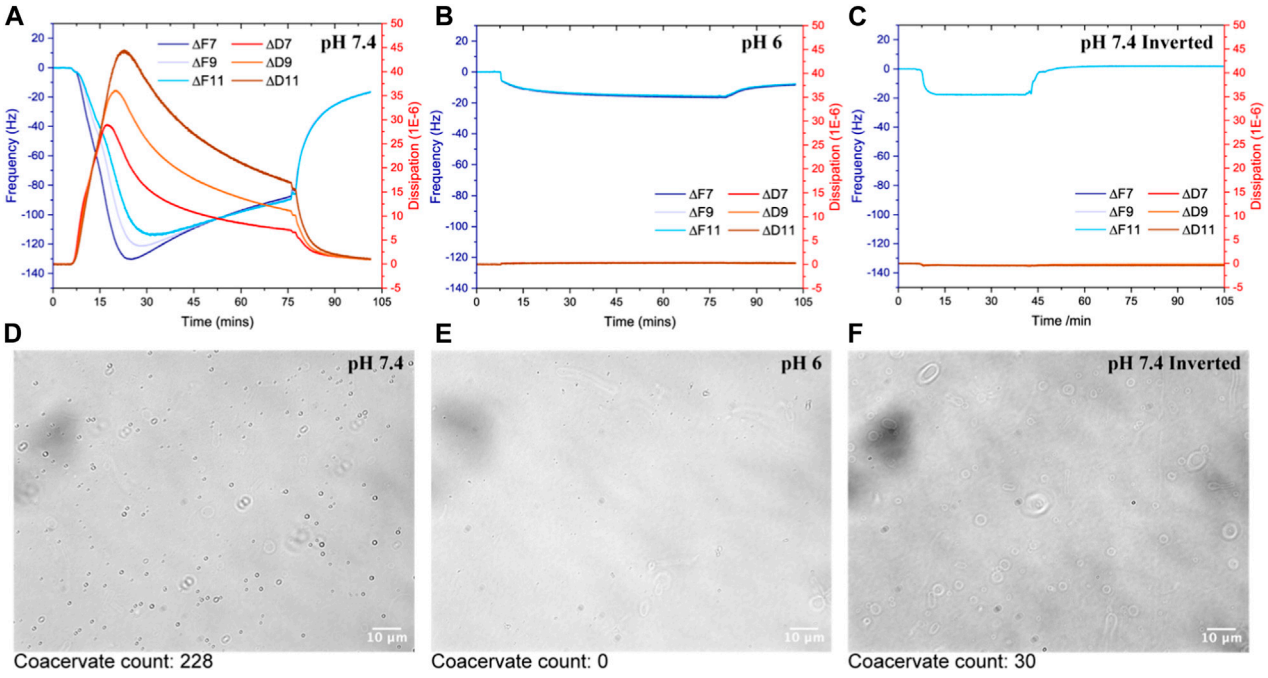

FIGURE 2
Interaction of HB*pep* on SLBs composed by POPC:POPG:Cholesterol at a 7:1:2 molar ratio in 10 mM phosphate buffer enriched with 154 mM NaCl at pH 6 **(A)** and pH 7.4 **(B)**. The QCM-D signals (Frequency in Hz and dissipation in ppm) are given as a function of time. In panel **(C)**, the E4 unit was flipped upside down to avoid sedimentation on the sensor surface. The flow was kept constant at 0.1 mL/min and all measurements were made at 25°C. **(D–F)** are DIC images of SLBs (POPC:POPG:Cholesterol at a 7:1:2 molar ratio) prepared using a solvent-assisted method on glass slides with experimental conditions kept consistent with those used in the QCM-D experiments depicted in **(A–C)**.

highest turbidity was observed at pH 7.4 which is close to the peptide's theoretical pI of 7.96 (Figure 1A). In acidic conditions and at pH values above 9, HB*pep* displayed minimal turbidity indicating its inability to coacervate and likely remained monomeric or resulted in low-level oligomerization. This pH-dependent behavior is due to the positive charges arising from the five histidine side groups when the pH is below its pK_{a2} of 6 (Saurabh et al., 2022), and to the negative charges arising from the tyrosine side groups when the pH is above its pK_{a2} of ~10 (Figure 1B), which result in charge-charge repulsion at these pH ranges. Since HB*pep* is acetyl-capped at the N-terminus and amidated on the C-terminus, we do not expect any end terminal charge contribution.

Similarly, a concentration-dependent behavior was observed when HB*pep* stock solutions were diluted into a buffer maintained at pH 7.4 (Figure 1C). An increase in turbidity (OD_{600}) correlated with an increase in HB*pep* concentration, with a detection threshold at 0.2 mg/mL and a peak turbidity signal at 0.6 mg/mL, beyond which the signal plateaued. At pH 6, where the peptide carries a net positive charge, DLS measurements suggest an oligomeric state for the peptide at 1 mg/mL (the oligomeric formation was confirmed by SANS data, data not shown) (Figure 1D). At pH 7.4, HB*pep* coacervate droplet sizes varied from 400–800 nm (Figure 1D), with size being both time- and concentration-dependent (Figure 1E). Micrometer-sized droplets were observed within 5 min for peptides at a concentration of 1 mg/mL, whereas sub-μm size particles were observed at a lower peptide concentration of 0.25 mg/mL (Figure 1D). Furthermore, μm size droplets sedimented over time, and the coalescing property of the coacervates became more discernible at higher peptide concentrations as seen from DIC microscopy images (Figures 1F–I). Based on the above results, a pH of 7.4 and 6 were chosen as the coacervating and non-coacervating pHs for the peptide, respectively. Since high peptide concentrations (>0.5 mg/mL) led to coacervate coalescence and a concomitant increase in droplet size, we determined 0.25 mg/mL as an appropriate peptide concentration to use for all further experiments as we expect the coacervate size to remain relatively stable under these conditions.

3.2 QCM-D

The interactions between HB*pep* coacervates and model cell membranes were followed via QCM-D on SLBs formed by vesicle fusion using vesicles composed by POPC:POPG:Cholesterol in a 7:1:2 molar ratio as a model of the charge in mammalian cell membranes (Virtanen et al., 1998). HB*pep* coacervates (0.25 mg/mL) were prepared and incubated for 5 min prior to addition to the SLBs. Analysis of the raw QCM-D data (Figures 2A, B) confirmed HB*pep* binding at pH 6, a condition where no significant coacervation occurs (Figures 1A, D). The observed QCM-D signal at acidic conditions closely resembles that of cell penetrating peptides such as penetratin (Hedegaard et al., 2018). Upon rinsing with buffer, partial desorption of HB*pep* occurred, which is also consistent with data observed for cell penetrating peptides (Hedegaard et al., 2018) (Figure 2B). In contrast, at pH 7.4, substantial adsorption of HB*pep* coacervates on the SLB coated SiO_2 sensor was observed (Figure 2A). The resulting QCM-D signal resembles the adsorption of lipid vesicles on SiO_2 and their

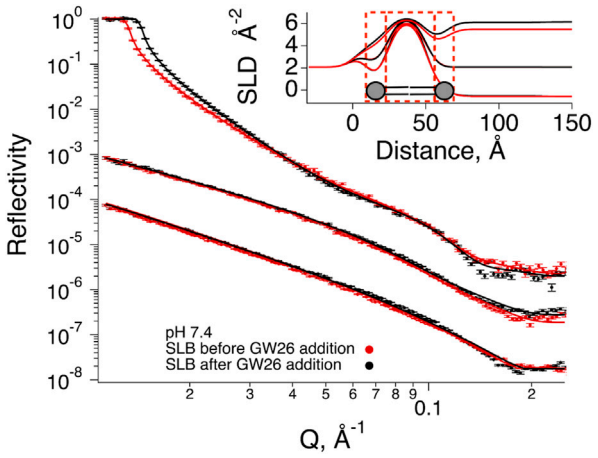

FIGURE 3
Neutron Reflection data for SLBs composed by POPC-d_{64}, DOPG-d_{66}, cholesterol-d_{45} (7:1:2 mol%) before (red) and after (black) exposure to HB*pep* at pH 7.4 buffer. The experimental data is given by symbols. Best fits (parameters in Table 1) are represented by solid lines. HB*pep* coacervates were prepared 5 min prior to the addition to the SLBs and incubated for 1 h 20 min. Rinsing with a peptide solution containing 1/10 of the original concentration at different contrasts was then performed to collect the three data sets shown in the figure. The cmSi and H_2O based data was offset for clarity. The inset gives SLD profiles for the best fit to the data.

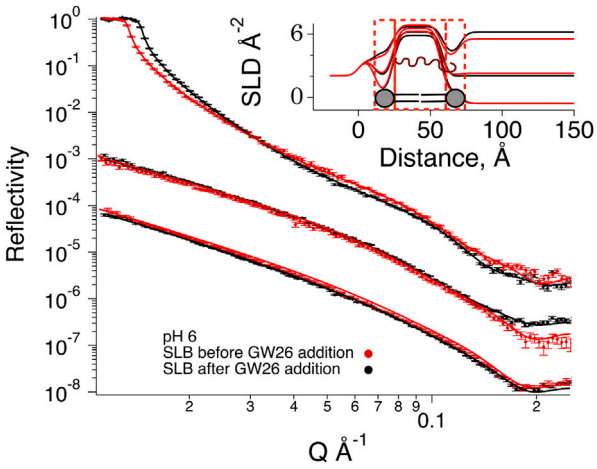

FIGURE 4
Neutron Reflection data for SLBs composed by POPC-d_{64}, DOPG-d_{66}, cholesterol-d_{45} (7:1:2 mol%) before (red) and after (black) exposure to HB*pep* at pH 6 buffer. The experimental data is given by symbols. Best fits (parameters in Table 1) are represented by solid lines. HB*pep* coacervates were prepared 5 min prior to the addition to the SLBs and incubated for 1 h 20 min. Rinsing with a peptide solution containing 1/10 of the original concentration at different contrasts was then performed to collect the three data sets shown in the figure. The cmSi and H_2O based data was offset for clarity. The inset gives SLD profiles for the best fit to the data.

eventual rupture, as evidenced by the sharp decrease in frequency and the increase in dissipation with time, followed by an inversion of the signals (increase in frequency and decrease in dissipation). Thus, it is likely that some of the µm-sized coacervates spread out on the SLB-coated sensor, mirroring what was observed by microscopy on glass slides (Figures 1H, I). We note that most of the adsorbed coacervates could be removed upon rinsing with buffer at pH 7.4 suggesting that the adsorption was largely reversible and could be due to simple droplet sedimentation.

In order to decouple the effect of molecular adsorption on the SLB and sedimentation, the QCM-D E4 unit was flipped upside down and the experiment at pH 7.4 was repeated (Figure 2C). In this case, a signal mirroring that measured at pH 6 was detected with full reversibility upon rinsing with a solution containing 1/10 of the original coacervate solution (i.e., 0.025 mg/mL) followed by excess buffer. Taken together, both peptide and coacervate adsorption takes place regardless of pH, but the adsorption is fully reversible only at neutral pH. The latter suggests that no major rearrangement of the lipid bilayer structure takes place due to peptide adsorption at pH 7.4. This was independently verified with SLBs prepared using a solvent-assisted method on glass slides that were imaged using DIC microscopy (Figures 2D–F). The experimental conditions were kept consistent with those used in the QCM-D experiments depicted in Figures 2A–C.

The DIC images reveal that at pH 7.4 in the upward position of the chamber (Figure 2D), more µm-sized coacervates adsorbed to the SLB compared to when the microfluidic chamber was set-up upside down (Figure 2F). At pH 6, no coacervates were observed (Figure 2E) as expected based on turbidity and DLS measurements (Figures 1A, D). A manual count (Supplementary Figures S3, S4) of the number of coacervates in each of the representative DIC images in Figures 2D–F revealed the count to be 228 for pH 7.4, 0 for pH 6 and 30 for upside down at pH 7.4. Since at pH 6 HB*pep* does not significantly coacervate into large droplets, the black dots observed in Figure 2E do not correspond to coacervates and are most likely pH dependent salt crystallization, or low-level oligomerization below the resolution limit of the microscope objective used.

3.3 Neutron reflectometry

Neutron reflection data were collected at three isotropic contrasts before and after exposure to 0.25 mg/mL HB*pep* at pH 6 (Figure 3) or pH 7.4 (Figure 4), and the data were fitted assuming a symmetric lipid bilayer structure (lipid heads–lipid tails–lipid heads). The thickness of the core lipid bilayer, the head groups and the roughness at pHs 6 and 7.4 are summarized in Table 1. The coverage was in both cases above 90%. The values in Table 1 compare well to those reported by Waldie et al (Waldie et al., 2018; Waldie et al., 2019) for which 30.9-33.5 Å thick core was measured for 10–40 mol% cholesterol in various phosphatidylcholine SLBs including POPC. The head group region was found to be 7-8 Å thick for PC-cholesterol (Waldie et al., 2018; Waldie et al., 2019). The larger headgroups [12.9 and 13.3 (±0.3) Å at pH 6 and pH 7.4, respectively] and headgroup hydration is thus expected from the presence of charged phosphatidylglycerol groups (Le Brun et al., 2014).

At pH 7.4 (where HB*pep* coacervation takes place), there were minimal changes in reflectivity (Figure 4). The small changes observed at low Q are simply due to small differences in the D_2O content in the buffer, typical when there is incomplete exchange upon flushing with buffer. There was though a very small increase in reflectivity mainly observable for the H_2O based

TABLE 1 Parameters for the best fits shown in Figures 3, 4.

	SLD ($^a10^{-6}$ Å^2)	Thickness (Å)	Coverage (%)	Roughness (Å)	Mean molecular area (Å$_2$)
pH 7,4					
SiO_2		10.2 ± 0.3		7.0 ± 0.5	
Head	1.95[a]	13.0 ± 0.2	46 ± 1	6.8 ± 0.4	53 ± 2
Tail	6.4 ± 0.1	29.0 ± 0.2	93 ± 1	6.8 ± 0.4	63 ± 1
Head	1.95[a]	13.0 ± 0.2	46 ± 1	6.8 ± 0.4	53 ± 2
After HB*pep* addition					
Head	1.95[a]	13[a]	39 ± 2	6.8[a]	63 ± 2
Tail	6.4[a]	29[a]	100 ± 1	6.8[a]	59 ± 1
Head	1.95[a]	13[a]	39 ± 2	6.8[a]	63 ± 2
Protein slab		69 ± 4	1.3 ± 0.2	6.8[a]	
pH 6					
SiO2		11.2 ± 0.2		3.7 ± 0.4	
Head	1.95[a]	12.5 ± 0.1	46 ± 1	5.4 ± 0.3	54 ± 2
Tail	7.02 ± 0.04	33.3 ± 0.2	90 ± 1	5.4 ± 0.3	58 ± 1
Head	1.95[a]	12.5 ± 0.1	46 ± 1	5.4 ± 0.3	54 ± 2
After HB*pep* addition					
Head	1.95[a]	10.7 ± 0.1	46 ± 1	3.8	65 ± 2
Tail	6.78 ± 0.03	*34.4* ± 0.3	96 ± 1	3.8	52 ± 1
Head	1.95[a]	10.7 ± 0.1	46 ± 1	3.8	65 ± 2
Protein slab		58 ± 5	2.6 ± 0.5	3.8	

[a]Fixed parameters.

Heads were co-fitted as symmetric across contrasts, roughness was co-fitted across layers and contrasts, tail SLD, was co-fitted across contrasts. The SLD, for D_2O corresponds to 85%–89% and 0.2% to 0.9% D_2O before and after peptide addition as determined by the position of the critical scattering angle.

buffer. These changes can be interpreted as an increase in the coverage or scattering length density (SLD) of the SLB. Indeed, upon co-refinement of the data using a four-layer model (lipid heads–tails–lipid heads–HB*pep*), a suitable fit was obtained assuming a constant layer thickness of the SLB but allowing for increase in the coverage of 7%. There was neither any significant peptide adsorption on top of the SLB, nor any significant drop in the SLD of the lipid bilayer region. During SLB formation by vesicle fusion, it is common that a small fraction of vesicles remain bound, these are hardly seen by NR (Lind et al., 2014). Together, these values suggest the rupture of a few vesicles that might have remained bound to the SLB after the rinsing step, and that there was neither significant peptide binding nor integration in the lipid bilayer, consistent with the QCM-D results (Figure 2C).

At pH 6, where HB*pep* remains mostly in the monomeric or oligomeric state (Figure 1E), significant changes in reflectivity were noticed at all contrasts besides the small changes observed at low Q for D_2O-based buffer due to incomplete exchange upon flushing with buffer. In particular, the cross over in the D_2O based buffer contrast suggest a change in the SLB structure/composition (Lind T. K. et al., 2015). Indeed, upon co-refinement of the data using a four-layer model (lipid heads–tails–lipid heads–HB*pep*), a suitable fit was obtained with a 1.4 Å increase in the lipid tail layer thicknesses, a lowering of 0.24×10^{-6} Å^{-2} in the lipid tail layer SLD, and a coverage increase by 6%. Together, these values point towards the integration of peptide in the layer. This corresponds to 5 % of the layer being composed of peptide and 95% of lipids. There was some peptide adsorption on top of the SLB, although minimal.

NR indicates that at conditions in which the peptide is cationic and does not form coacervates (i.e., at low pH), the peptide intercalates in the lipid bilayer, partially removing some lipids, a finding in agreement with observations for cationic peptides with antimicrobial capacity (Lind T. et al., 2015; Nielsen et al., 2019; Hedegaard et al., 2020). For neutral pH, where the peptide is largely uncharged and mainly present in the coacervate phase, minimal interaction was detected with the SLB. Instead, a slight increase in the coverage of the SLB was observed without affecting the lipid core SLD. This suggests that eventual non-fused lipid vesicles collapsed due to the presence of coacervates in the bulk phase.

3.4 MD simulations

Figures 5A–C presents comparative snapshots of the SLB before and after 200 ns of simulation at both neutral and acidic conditions. At neutral conditions, the HB*peps* predominantly form aggregates

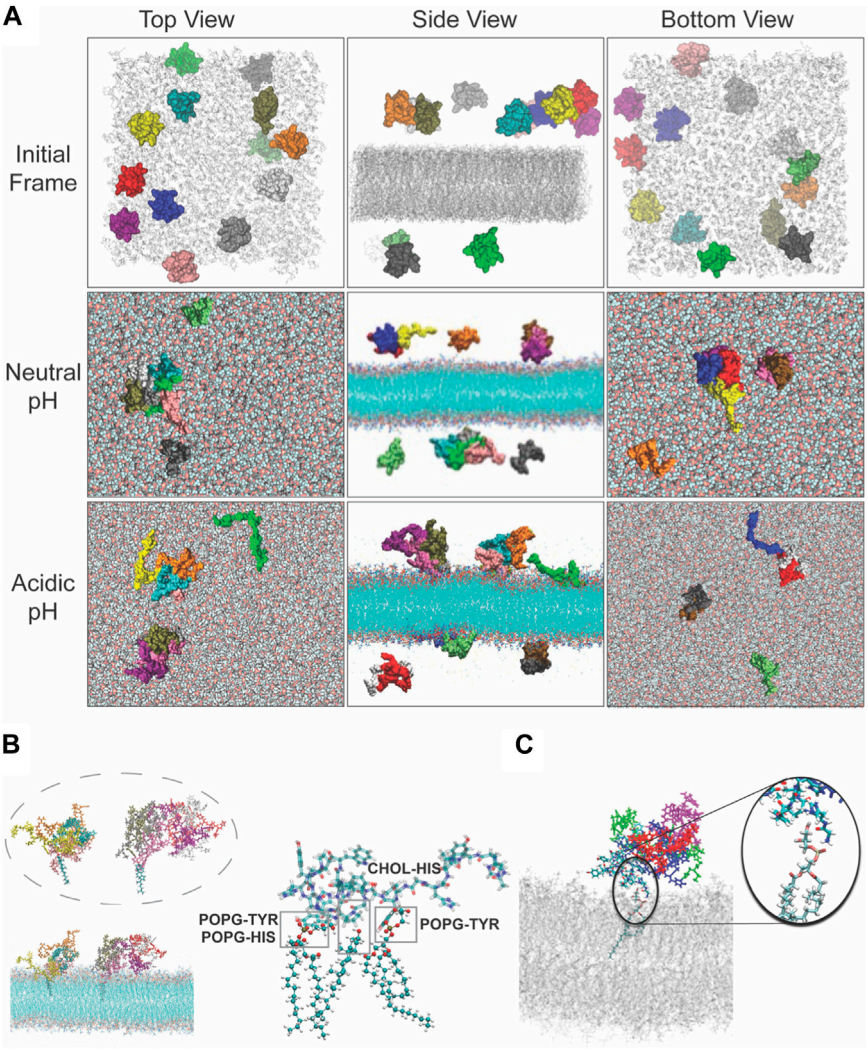

FIGURE 5
Interactions observed between the peptide and POPG or cholesterol during the molecular dynamics simulations under neutral and acidic conditions. **(A)** Top, side and bottom view of the model system at the beginning of the simulation where peptides were randomly placed at either side of the membrane in the solution. Peptides are shown in van der Waals representation and colored differently, and the lipid membrane is shown in grey. Top, middle and lower row give representative snapshot of the model under neutral or acidic conditions. Snapshot of the interactions observed between the peptide and POPG or cholesterol during the molecular dynamics simulations under **(B)** neutral and **(C)** acidic conditions (the middle structure highlights the interactions between residues and lipid headgroups under acidic conditions).

within the solution, consisting of clusters of 4–6 members, where they remain for the duration of the simulations. In acidic conditions, however, HB*peps* display a distinct behavior: they land on the surface of the bilayer either as individual entities or as small aggregates comprised of 2, 3 or 4 peptides, subsequently penetrating into the membrane core. Note that oligomeric formation agrees well with the DLS data presented in Figure 1D at acidic pH. Even though larger aggregates are not observed at neutral pH, all peptides in the simulation box form aggregates while only a few do form oligomers at acidic pH. The primary interactions between the HB*peps* and the bilayer is via His and the phosphate group of POPG or the aromatic ring of Tyr, Trp or His and the hydroxyl group of cholesterol, as depicted in Figure 5B. These observations indicate that charged lipids and cholesterol are crucial for facilitating the binding of HB*pep* to membranes, in agreement with findings from previous cell studies (Sun et al., 2023).

4 Conclusion

HB*pep* coacervates do not interact with the lipid membrane at neutral pH in the same manner as traditional cationic drug delivery systems or cell penetrating peptides. Our data indicate that at pH 6 HB*pep* does not coacervate but forms small oligomers with a positive net charge. In this case, the peptide is able to insert into the lipid bilayer of a model cell membrane as shown both by NR experiments and MD simulations. These interactions are both charge driven but also promoted by π-OH interactions with cholesterol. However, at physiological pH, where the peptide phase-separates into μm or sub-μm sized droplets, it does not strongly interact with the lipid membrane. This indicates that the cell entry mechanism of HB*pep* coacervates prior to cargo delivery in the cytoplasm differs from that of cell penetrating peptides or cationic drug delivery vehicles. On-going studies on the cellular

uptake mechanism of coacervates, investigated using electron microscopy and live cell imaging, suggest a non-canonical uptake pathway mediated by cholesterol and will be published in a separate article.

Data availability statement

The original contributions presented in the study are included in the article/Supplementary Material, further inquiries can be directed to the corresponding authors.

Author contributions

SG: Data curation, Formal Analysis, Investigation, Supervision, Writing–original draft, Writing–review and editing. FF: Data curation, Formal Analysis, Investigation, Writing–review and editing. JSMT: Data curation, Formal Analysis, Writing–review and editing. CD: Data curation, Formal Analysis, Investigation, Writing–original draft, Writing–review and editing. SM: Data curation, Formal Analysis, Writing–review and editing. AL: Data curation, Formal Analysis, Resources, Writing–review and editing. NY: Methodology, Resources, Writing–review and editing. MM: Methodology, Resources, Writing–review and editing. RR: Methodology, Resources, Writing–review and editing. TD: Methodology, Resources, Writing–review and editing. AM: Conceptualization, Funding acquisition, Resources, Supervision, Writing–review and editing. MC: Conceptualization, Data curation, Formal Analysis, Investigation, Supervision, Writing–original draft, Writing–review and editing.

Funding

The author(s) declare financial support was received for the research, authorship, and/or publication of this article. This research was funded by the Ministry of Education (MOE), Singapore, through an Academic Research Fund (AcRF) Tier 3 grant (Grant No. MOE 2019-T3-1-012). The operations of the Spatz neutron beam instrument and the National Deuteration Facility are partly supported by the National Collaborative Research Infrastructure Strategy—an initiative of the Australian Government. This publication is part of project number PID2022-137440NB-I00, funded by MCIN/AEI/10.13039/501100011033/FEDER, UE. MC thanks the Swedish Research Council (2018-04833 and 2018-03990), Biofilm Research Center for Biointerfaces (Malmö University) and Wennergren foundation for financial support.

Acknowledgments

We thank the NTU Optical Bio-Imaging Centre (NOBIC) at the Singapore Centre for Environmental Life Sciences Engineering (SCELSE), NTU for the use of DIC microscopes and Dr. Yong Hwee Foo for his help and suggestions with imaging. This research was undertaken on the SPATZ beamline at the Australian Centre for Neutron Scattering, part of ANSTO. We are thankful to ANSTO for this opportunity and for allowing us to use their facilities. CD acknowledges use of computing resources on HPC platforms granted via the UK High-End Computing Consortium for Biomolecular Simulation, HECBioSim (http://hecbiosim.ac.uk), supported by EPSRC (Grant No. EP/R029407/1). MC thanks the Swedish Research Council, Biofilm—Research center for Biointerfaces, and Wennergren foundation for funding.

Conflict of interest

The authors declare that the research was conducted in the absence of any commercial or financial relationships that could be construed as a potential conflict of interest.

Publisher's note

Supplementary material

The Supplementary Material for this article can be found online at: https://www.frontiersin.org/articles/10.3389/frsfm.2023.1339496/full#supplementary-material

References

Behzadi, S., Serpooshan, V., Tao, W., Hamaly, M. A., Alkawareek, M. Y., Dreaden, E. C., et al. (2017). Cellular uptake of nanoparticles: journey inside the cell. *Chem. Soc. Rev.* 46 (14), 4218–4244. doi:10.1039/c6cs00636a

Berendsen, H. J. C., Vanderspoel, D., and Vandrunen, R. (1995). Gromacs - a message-passing parallel molecular-dynamics implementation. *Comput. Phys. Commun.* 91 (1-3), 43–56. doi:10.1016/0010-4655(95)00042-e

Bergeron-Sandoval, L. P., Kumar, S., Heris, H. K., Chang, C. L. A., Cornell, C. E., Keller, S. L., et al. (2021). Endocytic proteins with prion-like domains form viscoelastic condensates that enable membrane remodeling. *Proc. Natl. Acad. Sci. U. S. A.* 118 (50), e2113789118. doi:10.1073/pnas.2113789118

Boeynaems, S., Holehouse, A. S., Weinhardt, V., Kovacs, D., Van Lindt, J., Larabell, C., et al. (2019). Spontaneous driving forces give rise to Protein– rna condensates with coexisting phases and complex material properties. *Proc. Natl. Acad. Sci.* 116 (16), 7889–7898. doi:10.1073/pnas.1821038116

Clifton, L. A., Campbell, R. A., Sebastiani, F., Campos-Teran, J., Gonzalez-Martinez, J. F., Bjorklund, S., et al. (2020). Design and use of model membranes to study biomolecular interactions using complementary surface-sensitive techniques. *Adv. Colloid Interface Sci.* 277, 102118. doi:10.1016/j.cis.2020.102118

Darden, T., York, D., and Pedersen, L. Particle Mesh Ewald: an N·Log(N) method for Ewald sums in large systems. *J. Chem. Phys.* 1993, 98 (12), 10089–10092. doi:10.1063/1.464397

Darwish, T. A., Luks, E., Moraes, G., Yepuri, N. R., Holden, P. J., and James, M. (2013). Synthesis of deuterated [D32]oleic acid and its phospholipid derivative [D64]dioleoyl-

Sn-Glycero-3-Phosphocholine. *J. Label. Comp. Radiopharm.* 56 (9-10), 520–529. doi:10.1002/jlcr.3088

Feller, S. E., Zhang, Y., Pastor, R. W., and Brooks, B. R. (1995). Constant pressure molecular dynamics simulation: the Langevin piston method. *J. Chem. Phys.* 103 (11), 4613–4621. doi:10.1063/1.470648

Ferhan, A. R., Yoon, B. K., Park, S., Sut, T. N., Chin, H., Park, J. H., et al. (2019). Solvent-assisted preparation of supported lipid bilayers. *Nat. Protoc.* 14 (7), 2091–2118. doi:10.1038/s41596-019-0174-2

Gabryelczyk, B., Cai, H., Shi, X., Sun, Y., Swinkels, P. J. M., Salentinig, S., et al. (2019). Hydrogen bond guidance and aromatic stacking drive liquid-liquid phase separation of intrinsically disordered histidine-rich peptides. *Nat. Commun.* 10 (1), 5465. doi:10.1038/s41467-019-13469-8

Gouveia, B., Kim, Y., Shaevitz, J. W., Petry, S., Stone, H. A., and Brangwynne, C. P. (2022). Capillary forces generated by biomolecular condensates. *Nature* 609 (7926), 255–264. doi:10.1038/s41586-022-05138-6

Gyanani, V., and Goswami, R. (2023). Key design features of lipid nanoparticles and electrostatic charge-based lipid nanoparticle targeting. *Pharmaceutics* 15 (4), 1184. doi:10.3390/pharmaceutics15041184

Harush-Frenkel, O., Rozentur, E., Benita, S., and Altschuler, Y. (2008). Surface charge of nanoparticles determines their endocytic and transcytotic pathway in polarized mdck cells. *Biomacromolecules* 9 (2), 435–443. doi:10.1021/bm700535p

Hedegaard, S. F., Bruhn, D. S., Khandelia, H., Cárdenas, M., and Nielsen, H. M. (2020). Shuffled lipidation pattern and degree of lipidation determines the membrane interaction behavior of a linear cationic membrane-active peptide. *J. Colloid Interface Sci.* 578, 584–597. doi:10.1016/j.jcis.2020.05.121

Hedegaard, S. F., Derbas, M. S., Lind, T. K., Kasimova, M. R., Christensen, M. V., Michaelsen, M. H., et al. (2018). Fluorophore labeling of a cell-penetrating peptide significantly alters the mode and degree of biomembrane interaction. *Sci. Rep.* 8 (1), 6327. doi:10.1038/s41598-018-24154-z

Herce, H. D., and Garcia, A. E. (2007). Cell penetrating peptides: how do they do it? *J. Biol. Phys.* 33 (5-6), 345–356. doi:10.1007/s10867-008-9074-3

Humphrey, W., Dalke, A., and Schulten, K. (1996). Vmd: visual molecular dynamics. *J. Mol. Graph.* 14 (1), 33–38. doi:10.1016/0263-7855(96)00018-5

Jo, S., Kim, T., Iyer, V. G., and Im, W. (2008). Charmm-gui: a web-based graphical user interface for charmm. *J. Comput. Chem.* 29 (11), 1859–1865. doi:10.1002/jcc.20945

Jo, S., Lim, J. B., Klauda, J. B., and Im, W. (2009). Charmm-gui membrane builder for mixed bilayers and its application to yeast membranes. *Biophysical J.* 97 (1), 50–58. doi:10.1016/j.bpj.2009.04.013

Jones, A. T., Gumbleton, M., and Duncan, R. (2003). Understanding endocytic pathways and intracellular trafficking: a prerequisite for effective design of advanced drug delivery systems. *Adv. Drug Deliv. Rev.* 55 (11), 1353–1357. doi:10.1016/j.addr.2003.07.002

Jorgensen, W. L., Chandrasekhar, J., Madura, J. D., Impey, R. W., and Klein, M. L. (1983). Comparison of simple potential functions for simulating liquid water. *J. Chem. Phys.* 79 (2), 926–935. doi:10.1063/1.445869

Karal, M. A., Levadnyy, V., Tsuboi, T. A., Belaya, M., and Yamazaki, M. (2015). Electrostatic interaction effects on tension-induced pore formation in lipid membranes. *Phys. Rev. E Stat. Nonlin Soft Matter Phys.* 92 (1), 012708. doi:10.1103/PhysRevE.92.012708

Kazmierczak, Z., Szostak-Paluch, K., Przybylo, M., Langner, M., Witkiewicz, W., Jedruchniewicz, N., et al. (2020). Endocytosis in cellular uptake of drug delivery vectors: molecular aspects in drug development. *Bioorg Med. Chem.* 28 (18), 115556. doi:10.1016/j.bmc.2020.115556

Kern, N. R., Lee, J., Choi, Y. K., and Im, W. (2023). Charmm-gui multicomponent assembler for modeling and simulation of complex multicomponent systems. *bioRxiv*, 2023.08.30.555590. doi:10.1101/2023.08.30.555590

Klauda, J. B., Venable, R. M., Freites, J. A., O'Connor, J. W., Tobias, D. J., Mondragon-Ramirez, C., et al. (2010). Update of the charmm all-atom additive force field for lipids: validation on six lipid types. *J. Phys. Chem. B* 114 (23), 7830–7843. doi:10.1021/jp101759q

Latham, A. P., and Zhang, B. (2022). Molecular determinants for the layering and coarsening of biological condensates. *Aggreg. Hob.* 3 (6), e306. doi:10.1002/agt2.306

Le Brun, A. P., Haigh, C. L., Drew, S. C., James, M., Boland, M. P., and Collins, S. J. (2014). Neutron reflectometry studies define prion protein N-terminal peptide membrane binding. *Biophysical J.* 107 (10), 2313–2324. doi:10.1016/j.bpj.2014.09.027

Le Brun, A. P., Huang, T.-Y., Pullen, S., Nelson, A. R., Spedding, J., and Holt, S. A. (2023). Spatz: the time-of-flight neutron reflectometer with vertical sample geometry at the opal research reactor. *J. Appl. Crystallogr.* 56 (1), 18–25. doi:10.1107/s1600576722010860x

Li, H., Robertson, A. D., and Jensen, J. H. (2005). Very fast empirical prediction and rationalization of protein pka values. *Proteins* 61 (4), 704–721. doi:10.1002/prot.20660

Lim, Z. W., Ping, Y., and Miserez, A. (2018). Glucose-responsive peptide coacervates with high encapsulation efficiency for controlled release of insulin. *Bioconjug Chem.* 29 (7), 2176–2180. doi:10.1021/acs.bioconjchem.8b00369

Lim, Z. W., Varma, V. B., Ramanujan, R. V., and Miserez, A. (2020). Magnetically responsive peptide coacervates for dual hyperthermia and chemotherapy treatments of liver cancer. *Acta Biomater.* 110, 221–230. doi:10.1016/j.actbio.2020.04.024

Lind, T., Darré, L., Domene, C., Urbanczyk-Lipkowska, Z., Cárdenas, M., and Wacklin, H. (2015). Antimicrobial peptide dendrimer interacts with phosphocholine membranes in a fluidity dependent manner: a neutron reflection study combined with molecular dynamics simulations. *Biochimica Biophysica Acta (BBA)-Biomembranes* 1848 (10), 2075–2084. doi:10.1016/j.bbamem.2015.05.015

Lind, T. K., Darre, L., Domene, C., Urbanczyk-Lipkowska, Z., Cardenas, M., and Wacklin, H. P. (2015). Antimicrobial peptide dendrimer interacts with phosphocholine membranes in a fluidity dependent manner: a neutron reflection study combined with molecular dynamics simulations. *Biochim. Biophys. Acta* 1848 (10), 2075–2084. doi:10.1016/j.bbamem.2015.05.015

Lind, T. K., Cárdenas, M., and Wacklin, H. P. (2014). Formation of supported lipid bilayers by vesicle fusion: effect of deposition temperature. *Langmuir* 30 (25), 7259–7263. doi:10.1021/la500897x

Lind, T. K., Skoda, M. W. A., and Cardenas, M. (2019). Formation and characterization of supported lipid bilayers composed of phosphatidylethanolamine and phosphatidylglycerol by vesicle fusion, a simple but relevant model for bacterial membranes. *ACS Omega* 4 (6), 10687–10694. doi:10.1021/acsomega.9b01075

Liu, J., Spruijt, E., Miserez, A., and Langer, R. (2023). Peptide-based liquid droplets as emerging delivery vehicles. *Nat. Rev. Mater.* 8 (3), 139–141. doi:10.1038/s41578-022-00528-8

Lu, T., Liese, S., Schoenmakers, L., Weber, C. A., Suzuki, H., Huck, W. T., et al. (2022). Endocytosis of coacervates into liposomes. *J. Am. Chem. Soc.* 144 (30), 13451–13455. doi:10.1021/jacs.2c04096

Martyna, G. J., Tobias, D. J., and Klein, M. L. (1994). Constant pressure molecular dynamics algorithms. *J. Chem. Phys.* 101 (5), 4177–4189. doi:10.1063/1.467468

Miyamoto, S., and Kollman, P. A. (1992). Settle: an analytical version of the shake and rattle algorithm for rigid water models. *J. Comput. Chem.* 13 (8), 952–962. doi:10.1002/jcc.540130805

Moir, M., Yepuri, N. R., Marshall, D. L., Blanksby, S. J., and Darwish, T. A. (2022). Synthesis of perdeuterated linoleic acid-D31 and chain deuterated 1-palmitoyl-2-linoleoyl-Sn-Glycero-3-Phosphocholine-D62. *Adv. Synthesis Catal.* 364 (21), 3670–3681. doi:10.1002/adsc.202200616

Nelson, A. (2006). Co-refinement of multiple-contrast neutron/X-ray reflectivity data using motofit. *J. Appl. Crystallogr.* 39 (2), 273–276. doi:10.1107/s0021889806005073

Nelson, A. R. J., and Prescott, S. W. (2019). Refnx: neutron and X-ray reflectometry analysis in Python. *J. Appl. Crystallogr.* 52 (1), 193–200. doi:10.1107/S1600576718017296

Nielsen, J. E., Lind, T. K., Lone, A., Gerelli, Y., Hansen, P. R., Jenssen, H., et al. (2019). A biophysical study of the interactions between the antimicrobial peptide indolicidin and lipid model systems. *Biochimica Biophysica Acta (BBA)-Biomembranes* 1861 (7), 1355–1364. doi:10.1016/j.bbamem.2019.04.003

Noskov, S. Y., Berneche, S., and Roux, B. (2004). Control of ion selectivity in potassium channels by electrostatic and dynamic properties of carbonyl ligands. *Nature* 431 (7010), 830–834. doi:10.1038/nature02943

Phillips, J. C., Braun, R., Wang, W., Gumbart, J., Tajkhorshid, E., Villa, E., et al. (2005). Scalable molecular dynamics with namd. *J. Comput. Chem.* 26 (16), 1781–1802. Research Support, N.I.H., Extramural Research Support, Non-U.S. Gov't Research Support, U.S. Gov't, P.H.S. doi:10.1002/jcc.20289

Recsei, C., Russell, R. A., Cagnes, M., and Darwish, T. (2023). Deuterated squalene and sterols from modified Saccharomyces cerevisiae. *Org. Biomol. Chem.* 21 (32), 6537–6548. doi:10.1039/d3ob00754e

Rehman, Z. u., Zuhorn, I. S., and Hoekstra, D. (2013). How cationic lipids transfer nucleic acids into cells and across cellular membranes: recent advances. *J. Control. Release* 166 (1), 46–56. doi:10.1016/j.jconrel.2012.12.014

Rey, J., Murail, S., de Vries, S., Derreumaux, P., and Tuffery, P. (2023). Pep-Fold4: a ph-dependent force field for peptide structure prediction in aqueous solution. *Nucleic acids Res.* 51 (W1), W432–W437. doi:10.1093/nar/gkad376

Saurabh, S., Kalonia, C., Li, Z., Hollowell, P., Waigh, T., Li, P., et al. (2022). Understanding the stabilizing effect of histidine on mab aggregation: a molecular dynamics study. *Mol. Pharm.* 19 (9), 3288–3303. doi:10.1021/acs.molpharmaceut.2c00453

Sebastiani, F., Yanez Arteta, M., Lerche, M., Porcar, L., Lang, C., Bragg, R. A., et al. (2021). Apolipoprotein E binding drives structural and compositional rearrangement of mrna-containing lipid nanoparticles. *ACS Nano* 15 (4), 6709–6722. doi:10.1021/acsnano.0c10064

Shebanova, A., Perrin, Q., Gudlur, S., Sun, Y., Lim, Z. W., Sun, R., et al. (2022). Cellular uptake of his-rich peptide coacervates occurs by a macropinocytosis-like mechanism. *bioRxiv*, 502757. 2022.2008. 2004. doi:10.1101/2022.08.04.502757

Spleis, H., Sandmeier, M., Claus, V., and Bernkop-Schnurch, A. (2023). Surface design of nanocarriers: key to more efficient oral drug delivery systems. *Adv. Colloid Interface Sci.* 313, 102848. doi:10.1016/j.cis.2023.102848

Stewart, M. P., Langer, R., and Jensen, K. F. (2018). Intracellular delivery by membrane disruption: mechanisms, strategies, and concepts. *Chem. Rev.* 118 (16), 7409–7531. doi:10.1021/acs.chemrev.7b00678

Sun, Y., Lau, S. Y., Lim, Z. W., Chang, S. C., Ghadessy, F., Partridge, A., et al. (2022). Phase-separating peptides for direct cytosolic delivery and redox-activated release of macromolecular therapeutics. *Nat. Chem.* 14 (3), 274–283. doi:10.1038/s41557-021-00854-4

Sun, Y., Xu, X., Chen, L., Chew, W. L., Ping, Y., and Miserez, A. (2023). Redox-responsive phase-separating peptide as a universal delivery vehicle for crispr/cas9 genome editing machinery. *ACS Nano* 17 (17), 16597–16606. doi:10.1021/acsnano.3c02669

Tan, Y., Hoon, S., Guerette, P. A., Wei, W., Ghadban, A., Hao, C., et al. (2015). Infiltration of chitin by protein coacervates defines the squid beak mechanical gradient. *Nat. Chem. Biol.* 11 (7), 488–495. doi:10.1038/nchembio.1833

Thoren, P. E., Persson, D., Lincoln, P., and Norden, B. (2005). Membrane destabilizing properties of cell-penetrating peptides. *Biophys. Chem.* 114 (2-3), 169–179. doi:10.1016/j.bpc.2004.11.016

Tufféry, P., and Derreumaux, P. (2023). A refined ph-dependent coarse-grained model for peptide structure prediction in aqueous solution. *Front. Bioinform* 3, 1113928. doi:10.3389/fbinf.2023.1113928

Vedadghavami, A., Zhang, C., and Bajpayee, A. G. (2020). Overcoming negatively charged tissue barriers: drug delivery using cationic peptides and proteins. *Nano Today* 34, 100898. doi:10.1016/j.nantod.2020.100898

Verlet, L. (1967). Computer" experiments" on classical fluids. I. Thermodynamical properties of Lennard-Jones molecules. *Phys. Rev.* 159 (1), 98–103. doi:10.1103/physrev.159.98

Virtanen, J. A., Cheng, K. H., and Somerharju, P. (1998). Phospholipid composition of the mammalian red cell membrane can Be rationalized by a superlattice model. *Proc. Natl. Acad. Sci.* 95 (9), 4964–4969. doi:10.1073/pnas.95.9.4964

Waldie, S., Lind, T. K., Browning, K., Moulin, M., Haertlein, M., Forsyth, V. T., et al. (2018). Localization of cholesterol within supported lipid bilayers made of a natural extract of tailor-deuterated phosphatidylcholine. *Langmuir* 34 (1), 472–479. doi:10.1021/acs.langmuir.7b02716

Waldie, S., Moulin, M., Porcar, L., Pichler, H., Strohmeier, G. A., Skoda, M., et al. (2019). The production of matchout-deuterated cholesterol and the study of bilayer-cholesterol interactions. *Sci. Rep.* 9 (1), 5118. doi:10.1038/s41598-019-41439-z

Wang, J., Choi, J. M., Holehouse, A. S., Lee, H. O., Zhang, X., Jahnel, M., et al. (2018). A molecular grammar governing the driving forces for phase separation of prion-like rna binding proteins. *Cell* 174 (3), 688–699.e16. doi:10.1016/j.cell.2018.06.006

Wang, Z., Yang, C., Guan, D., Li, J., and Zhang, H. (2023). Cellular proteins act as surfactants to control the interfacial behavior and function of biological condensates. *Dev. cell* 58 (11), 919–932.e5. doi:10.1016/j.devcel.2023.04.004

Welsh, T. J., Krainer, G., Espinosa, J. R., Joseph, J. A., Sridhar, A., Jahnel, M., et al. (2022). Surface electrostatics govern the emulsion stability of biomolecular condensates. *Nano Lett.* 22 (2), 612–621. doi:10.1021/acs.nanolett.1c03138

Wu, E. L., Cheng, X., Jo, S., Rui, H., Song, K. C., Dávila-Contreras, E. M., et al. (2014). Charmm-gui membrane builder toward realistic biological membrane simulations. *J. Comput. Chem.* 35 (27), 1997–2004. doi:10.1002/jcc.23702

Yuan, F., Alimohamadi, H., Bakka, B., Trementozzi, A. N., Day, K. J., Fawzi, N. L., et al. (2021). Membrane bending by protein phase separation. *Proc. Natl. Acad. Sci. U. S. A.* 118 (11), e2017435118. doi:10.1073/pnas.2017435118